Scholars Journal of Physics, Mathematics and Statistics

OPEN ACCESS

Abbreviated Key Title: Sch J Phys Math Stat
ISSN 2393-8056 (Print) | ISSN 2393-8064 (Online)
Journal homepage: https://saspublishers.com

First Demonstration of Lead-Free Double Perovskite Cs_2NaBiI_6 as A Dual-Function Electrode for High-Performance, Long-Life Photo-Rechargeable Lithium-Ion Batteries with Superior Solar-To-Power Conversion

Muhammad Talha Bin Zubair[1], Waheed Zaman Khan[2*], Hasnain Abbas[1], Muhammad Asif[1], Saeed Ahmad[5], Muhammad Abdullah[6], Muhammad Adnan[7], Hajra Zafar[8], Ijaz Ahmad[2], Safeer Ul Islam[2]

[1]Department of Chemistry, University of Education, Lahore DG Khan Campus, Punjab 32200, Pakistan
[2]Department of Physics, Division of Science and Technology, University of Education, Lahore, Punjab 54770, Pakistan
[5]Department of Physics, Abdul Wali Khan University Mardan, Khyber Pakhtunkhwa, Pakistan
[6]Department of Physics, Hazara University, Mansehra 21300, KPK, Pakistan
[7]Department of Chemical, Polymer and Composite Materials Engineering, University of Engineering and Technology, Lahore, Pakistan
[8]Department of Chemistry, University of Gujrat, Punjab 50700, Pakistan

DOI: https://doi.org/10.36347/sjpms.2025.v12i08.002 | **Received:** 12.07.2025 | **Accepted:** 31.08.2025 | **Published:** 13.09.2025

***Corresponding author:** Waheed Zaman Khan
Department of Physics, Division of Science and Technology, University of Education, Lahore, Punjab 54770, Pakistan

Abstract | **Original Research Article**

A significant advance in solar energy harvesting and efficient storage can be achieved by developing integrated devices that perform both functions simultaneously. In this study, we present the first successful use of the lead-free double perovskite halide Cs_2NaBiI_6 as both electrode and photoelectrode in lithium-ion photobatteries (PHBATs). The Cs_2NaBiI_6 electrode exhibits outstanding electrochemical performance, delivering an initial specific capacity of 450 mAh g^{-1} and maintaining 150 mAh g^{-1} after 90 cycles, with remarkable stability even after 500 cycles. Ex situ X-ray diffraction analysis reveals a two-step lithium storage mechanism: reduction of Bi^{3+} to metallic bismuth (Bi^0), followed by alloying with lithium to form LiBi and Li_3Bi phases. Operated as a photo-rechargeable battery, the PHBAT achieves a peak light-to-power conversion efficiency of 0.27% under 1 sun illumination—among the highest reported for lithium-ion perovskite photobatteries. Chronoamperometric measurements under alternating dark and light conditions confirm enhanced current generation and sustained capacity under illumination, underscoring the role of photogenerated carriers. Demonstrating practical utility, the device can power a 1.5 V digital stopwatch solely using solar energy. Compared to $Cs_3Bi_2I_9$-based systems, the Cs_2NaBiI_6 PHBAT offers higher specific capacity, superior rate capability, and enhanced cycling stability. These results position lead-free Cs_2NaBiI_6 as a highly promising, eco-friendly candidate for next-generation photo-rechargeable lithium-ion energy storage, enabling cost-effective, fully integrated solar-powered devices.

Keywords: Double perovskite, lead-free perovskite, Cs_2NaBiI_6, photo-rechargeable battery, photobattery, lithium-ion battery, energy storage, solar energy harvesting, electrochemical performance, light conversion efficiency.

1. INTRODUCTION

The global surge in energy consumption has catalyzed a search for materials that can both capture and store energy within a single, unified device [1–3]. Rather than relying on separate systems for energy harvesting and storage, recent advances focus on embedding light-absorbing photovoltaic components directly into batteries, creating what are known as photobatteries (PHBATs) [4,5]. While conventional setups simply connect solar cells and batteries in series, the true innovation lies in engineering a device where the same material plays both roles. Such an integrated solution promises significantly greater energy density per unit mass and volume, which is particularly crucial for next-generation portable and wearable electronics [6].

The original concept of the photobattery dates back to 1976 [7], but the progress was hampered for

decades by the lack of materials that could simultaneously serve as efficient solar absorbers and effective lithium-ion hosts. As a result, the power conversion efficiency of early devices remained disappointingly low [8,9]. However, a new wave of research has recently revitalized the field. Recent publications have reported substantial progress, including "first-charge" light conversion efficiencies (LCEs) in PHBATs approaching the 1% mark—a dramatic improvement over the earliest attempts [6,10–14].

Metal halide perovskites have emerged as especially promising for PHBAT applications [2,8]. Their unique crystal structure yields strong optical absorption, efficient separation and transport of photo-generated charge carriers, and a remarkable defect tolerance that allows for stable ion intercalation [15,16]. Despite these advantages, the widespread use of conventional perovskites is limited by concerns over lead toxicity and the inherent instability of their active layers. Addressing these issues has motivated the search for lead-free perovskite variants, as well as hybrid nanostructured materials and core–shell architectures, all aiming to enhance both stability and performance [38,39,41].

Recent research has demonstrated that nanotechnology-driven modifications—such as nanocrystal engineering, surface passivation, and compositional tuning—can significantly improve the efficiency, stability, and storage capacity of perovskite-based energy devices [38,40]. For example, strategies using double perovskite structures and core–shell nanocrystals have shown improved moisture and thermal stability, while also facilitating more robust charge transport and reduced defect densities [40,41]. Density functional theory (DFT) calculations further underpin these innovations, allowing for rational materials discovery, prediction of optoelectronic behavior, and environmental impact modeling of next-generation perovskite systems [39,42].

An alternative solution is offered by the family of double perovskites. These materials feature a modified perovskite architecture, where the lead ions (Pb^{2+}) in the traditional ABX_3 structure are systematically replaced by a combination of monovalent and trivalent metal cations [18]. This results in a vast structural and compositional diversity, with the general formula $A_2BIBIIIX_6$, where A represents large cations (e.g., Cs^+, Rb^+), BI are monovalent metals (such as Na^+, K^+, Li^+, Ag^+, Cu^+), and BIII are trivalent metals (e.g., In^{3+}, Bi^{3+}, Sb^{3+}) [19,20]. Although double perovskite halides have found their place in solar cell research [21,22], their role as electrode materials in lithium-ion batteries is still emerging [23,24]. Only a handful of double perovskite-based lithium-ion batteries have been demonstrated, with examples such as $Cs_2NaBiCl_6$ showing stable capacities near 300 $mAhg^{-1}$ with excellent Coulombic efficiency [24], and $Cs_2AgBiBr_6$ being utilized for solar energy storage within more complex photoelectrochemical systems [25].

At the same time, efforts are underway to use advanced computational and experimental approaches to tailor the optoelectronic and thermoelectric properties of double perovskites, making them increasingly viable for both solar cell and energy storage applications [39,42]. For instance, novel compositions such as Rb_2TlSbX_2 and $CsPbX_3/Cs_2SnX_6$ core–shell structures have been theoretically predicted and experimentally verified to deliver superior light absorption, charge carrier mobility, and long-term device robustness in diverse environments [39,40].

In this work, we demonstrate for the first time the use of a double perovskite—specifically, Cs_2NaBiI_6—as the functional layer in a lithium-ion PHBAT. This compound was selected due to its favorable properties, including a narrow band gap suitable for visible light absorption, impressive stability against moisture and oxygen, and the ability to reversibly intercalate lithium ions without structural degradation. Our investigations reveal that lithium-ion batteries based on Cs_2NaBiI_6 achieve a high initial specific capacity of 450 $mAhg^{-1}$, maintain 150 $mAhg^{-1}$ after 90 cycles, and continue to function, though at a lower capacity, beyond 500 cycles. Importantly, the photobattery configuration based on this material exhibited a "first-charge" light conversion efficiency of 0.27%, surpassing many other known photoelectrodes. For comparison, this LCE is higher than that of commonly studied V_2O_5 photocathodes in lithium-ion batteries (0.22%) [14], and exceeds the efficiency observed for MoS_2/ZnO photocathodes used in zinc-ion batteries under standard illumination conditions (0.2%) [26].

2. METHODS

2.1. Materials

High-purity reagents were utilized throughout all experimental procedures to ensure reliable synthesis and device fabrication. Bismuth iodide (BiI_3, 99.99%), cesium iodide (CsI, 99.9% trace metals basis), and sodium iodide (NaI) were sourced from Sigma-Aldrich and used as received. The solvent N-methyl-2-pyrrolidone (NMP, 99.5%), along with copper foil (for use as an electrode substrate), poly(vinylidene fluoride) (PVDF), and [6,6]-phenyl C_{61} butyric acid methyl ester (PCBM), were likewise obtained from Sigma-Aldrich. Lithium metal foil, as well as the 1 M lithium hexafluorophosphate ($LiPF_6$) electrolyte in a mixture of ethylene carbonate (EC) and dimethyl carbonate (DMC) with 5% fluoroethylene carbonate (FEC), and Whatman GF/A filter papers, were purchased from DoDochem. Conductive carbon (Super P) was procured from Timcal, while the carbon felt (CF, Sigracet GDL 39 AA carbon graphite paper) was purchased from Fuel Cell Store. All chemicals were utilized without further purification unless otherwise specified.

2.2. Synthesis of Cs_2NaBiI_6 Double Perovskite

The target double perovskite halide, Cs_2NaBiI_6, was synthesized using a robust one-step hydrothermal approach [37]. In a typical synthesis, stoichiometric amounts of CsI, NaI, and BiI_3 were dissolved in 5 mL of 9 M hydroiodic acid (HI, 47 wt% in water) to achieve a final concentration of 0.2 M for Cs_2NaBiI_6. After a brief period of stirring to ensure homogeneous mixing, the resulting solution was transferred into a Teflon-lined stainless-steel autoclave. The hydrothermal reaction was then conducted at 120 °C for 2 hours. Upon completion, the autoclave was allowed to cool to room temperature gradually over 10–12 hours. This slow cooling step was critical for the formation of well-defined, deep red-colored Cs_2NaBiI_6 crystals.

The harvested crystals underwent successive washing steps to remove unreacted precursors and byproducts: alternating rinses with deionized water (DI), hexane, and isopropanol (IPA) were performed, followed by centrifugation until the supernatant ran clear. The final purified product was obtained by drying the washed crystals in an oven at 40 °C. Structural characterization was performed using X-ray diffraction (XRD), with results compared to established standards and previously reported data to confirm phase purity and crystallinity (see Figure S9).

2.3. Fabrication of Electrodes on Copper Foil

To prepare electrodes for standard lithium-ion battery testing, 70 mg of synthesized Cs_2NaBiI_6 powder was combined with 20 mg of conductive carbon (Super P) and 10 mg of PVDF binder. The mixture was thoroughly hand-ground with a pestle and mortar to ensure uniformity. This powder blend was then suspended in 500 µL of NMP solvent and stirred overnight, producing a viscous slurry. The slurry was evenly spread onto copper foil using the doctor blade technique, producing a film of consistent thickness. The coated foil was dried in an oven at 80 °C for 12 hours to evaporate the solvent fully. Circular electrode disks of 17 mm diameter were then punched from the dried film, with a typical mass loading of Cs_2NaBiI_6 between 1.1 and 1.3 mg/cm².

2.4. Fabrication of Electrodes on Carbon Felt

For the photobattery studies, electrodes were also fabricated using carbon felt (CF) as the current collector, taking advantage of its conductivity and transparency to light. First, 20 mg of PCBM was dissolved in 1 mL of NMP by sonication for 1 hour to ensure complete dissolution. Next, 70 mg of Cs_2NaBiI_6 powder was added, and the mixture was stirred for 12 hours at 1500 rpm. Subsequently, 10 mg of PVDF was incorporated as a binder, with further stirring for 1 hour. Discs of carbon felt (17 mm diameter) were then prepared and 40 µL of the electrode slurry was drop-cast onto each disc. The electrodes were left to dry overnight at 80 °C, resulting in a uniform layer of active material.

2.5. Photobattery Assembly

All assembly steps for photobattery devices were performed inside an argon-filled glovebox to prevent unwanted reactions with moisture or oxygen. A custom CR2450 coin cell case was adapted for photocharging experiments by creating a 9 mm diameter hole in the center of the cell cap and sealing it with a transparent glass substrate, enabling controlled illumination. The cell was constructed by stacking the following layers: the carbon felt/Cs_2NaBiI_6 photoelectrode, a glass fiber separator (Whatman GF/D) soaked in the 1 M $LiPF_6$ in EC/DMC (1:1 by volume) with 5% FEC electrolyte, and a lithium metal foil (0.45 mm thick) as the counter electrode. The photoelectrodes typically had an areal mass loading of Cs_2NaBiI_6 in the range of 1.1 to 1.5 mg/cm².

The completed photobattery (PHBAT) thus featured a layer-by-layer configuration: CF current collector/Cs_2NaBiI_6 photoactive layer/separator with electrolyte/Li metal anode. A xenon lamp (Perfect PLS-SXE300), providing simulated sunlight at 1 sun intensity (AM 1.5G), was employed as the illumination source for all photocharging experiments unless otherwise specified.

3. RESULTS AND DISCUSSION

The successful synthesis of the double-perovskite halide Cs_2NaBiI_6 was achieved through a single-step hydrothermal method, as described in detail in the Methods section. This approach yields a product that is both structurally and chemically robust, as confirmed through a comprehensive suite of characterization techniques.

3.1. Crystal Structure and Morphology

X-ray crystallography reveals that Cs_2NaBiI_6 adopts a three-dimensional cubic perovskite framework, as depicted in Figure 1a. The crystal lattice is characterized by corner-sharing NaI_6 and BiI_6 octahedra extending in all three spatial dimensions, which is typical for perovskite-type materials and is crucial for facilitating both ionic mobility and electronic transport. The high degree of structural symmetry associated with this arrangement can promote stability and performance in device contexts.

To further investigate the morphology, field-emission scanning electron microscopy (FESEM) was employed. The resulting images (Figure 1b) reveal that the synthesized Cs_2NaBiI_6 consists of well-faceted, shuttle-like microcrystals. These individual crystallites are several micrometers in both length and width, and display smooth surfaces and sharply defined edges—an indication of high crystallinity and effective control over the growth process.

3.1.1. Phase Purity and Structural Analysis

To assess the phase purity and confirm the formation of the targeted double perovskite, powder X-ray diffraction (XRD) was performed (Figure 1c). The

observed diffraction peaks align closely with those previously reported for Cs_2NaBiI_6 [27], as well as the structurally related $(MA)_2AgBiI_6$ double perovskite [28]. Four prominent peaks at 13.8°, 25.2°, 27.6°, and 32.3° are clearly present, corresponding to the major reflections of the double perovskite structure. The lack of significant signals from starting materials or secondary phases, aside from minor traces of BiI_3 and $Cs_3Bi_2I_9$ as identified, indicates high phase purity. Further symmetry analysis places the structure in the hexagonal space group $P6_3/mmc$, a finding that is consistent with the broader family of double perovskites.

3.1.2. Optical Properties

The optical absorption characteristics of Cs_2NaBiI_6 were investigated via UV–vis spectroscopy (Figure 1d). The material exhibits strong and broad absorption across the visible region, with a particularly intense excitonic feature centered around 500 nm. Analysis using Tauc plots reveals that Cs_2NaBiI_6 possesses a direct band gap of approximately 2.12 eV and an indirect band gap near 1.42 eV, in close agreement with previously reported values [27–29]. These electronic properties make Cs_2NaBiI_6 well-suited for harvesting both ultraviolet and a significant portion of the visible spectrum—wavelengths extending up to nearly 600 nm.

3.1.3. Device Integration

A schematic illustration (see Figure S1) highlights the integration of Cs_2NaBiI_6 as the active layer within the photobattery (PHBAT) architecture. The combination of well-defined crystal structure, high optical absorption, and phase purity underpins the suitability of Cs_2NaBiI_6 for advanced energy storage and photocharging applications.

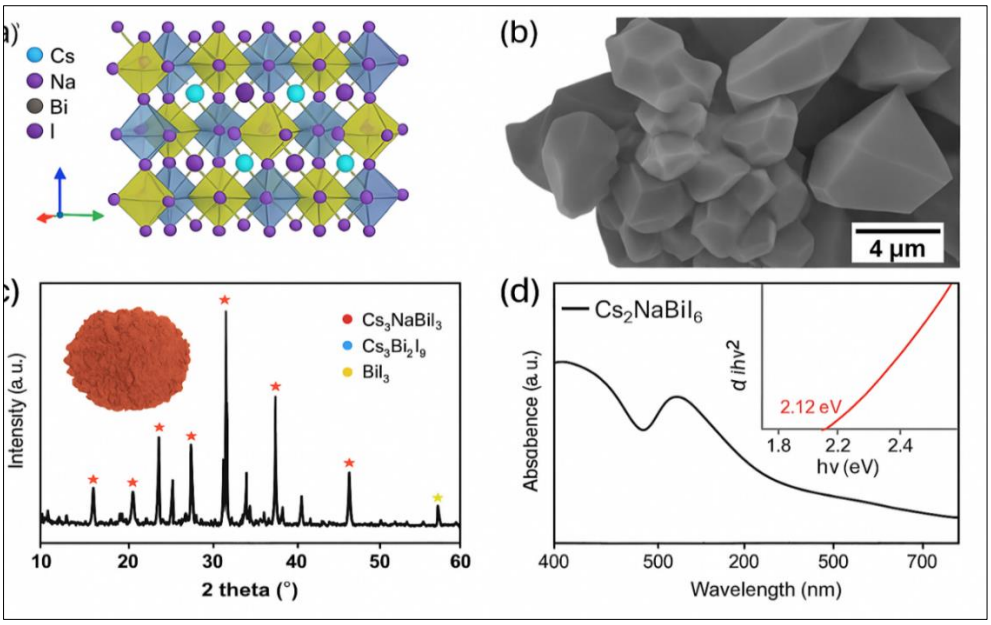

Figure 1: Structural, Morphological, and Optical Characterization of Cs_2NaBiI_6 Double Perovskite (a) Schematic crystal structure of Cs_2NaBiI_6, illustrating the 3D network of corner-sharing NaI_6 and BiI_6 octahedra with Cs^+ ions occupying the interstitial sites. (b) Representative SEM image showing the morphology of micron-sized, faceted Cs_2NaBiI_6 microcrystals. (c) Powder XRD pattern of as-synthesized Cs_2NaBiI_6, with characteristic peaks labeled; inset: photograph of the deep red microcrystalline powder. (d) UV–vis absorption spectrum of Cs_2NaBiI_6, with the Tauc plot inset indicating a direct optical band gap of 2.12 eV.

3.2. Electrochemical Performance of Cs_2NaBiI_6 in Conventional Lithium-Ion Cells

To benchmark the lithium-ion storage properties of Cs_2NaBiI_6 independently from its photoactive function, standard CR2450-type coin cells were assembled using Cs_2NaBiI_6 as the active material and metallic lithium foil serving as both the counter and reference electrode. The fabrication protocol followed established methods [6] and is described in detail in the Methods section.

The electrochemical behavior was systematically investigated by galvanostatic charge–discharge (GCD) measurements and cyclic voltammetry (CV) within a voltage window of 2.50–0.01 V versus Li/Li^+ (see Figure 2a and 2b). The initial five cycles were conducted at a low current density of 50 mA g^{-1} to facilitate the formation of a stable electrode/electrolyte interface, followed by subsequent cycling at 100 mA g^{-1}. The first discharge delivered a high specific capacity of 460 mA h g^{-1}, indicating robust lithium insertion into the Cs_2NaBiI_6 matrix.

A notable, though expected, decrease in capacity was observed following the initial cycle, attributed to the irreversible processes common in bismuth-based electrodes. These include the formation of the solid electrolyte interphase (SEI) and the reduction of Bi^{3+} ions to metallic Bi^0 within the perovskite host lattice [17]. Such irreversible phenomena have been

previously reported for bismuth-containing compounds in lithium-ion batteries [17,30] and are a known feature of bismuth-based electrochemical systems [31].

Despite the initial loss, the electrode demonstrated remarkable long-term stability, maintaining a specific capacity of 150 mA h g^{-1} even after 90 cycles at 100 mA g^{-1} (see Figure 2c). This stability is indicative of both the robust crystal structure of Cs_2NaBiI_6 and the formation of a passivating interface that supports repeated lithium insertion/extraction. Extended cycling data, presented in Figure S2, further confirm the durability of the system over 500 cycles, with negligible degradation in capacity—a highly promising result for practical applications.

Additional rate capability tests (Figure 2d) were conducted to evaluate the electrode's performance under varying current densities, and the results reveal consistent and efficient lithium-ion transport, with only minor decreases in capacity at higher rates. Notably, measurement errors for cycle stability and rate performance (capacity and efficiency) were less than ±0.1%, highlighting the reproducibility and reliability of the experimental procedure.

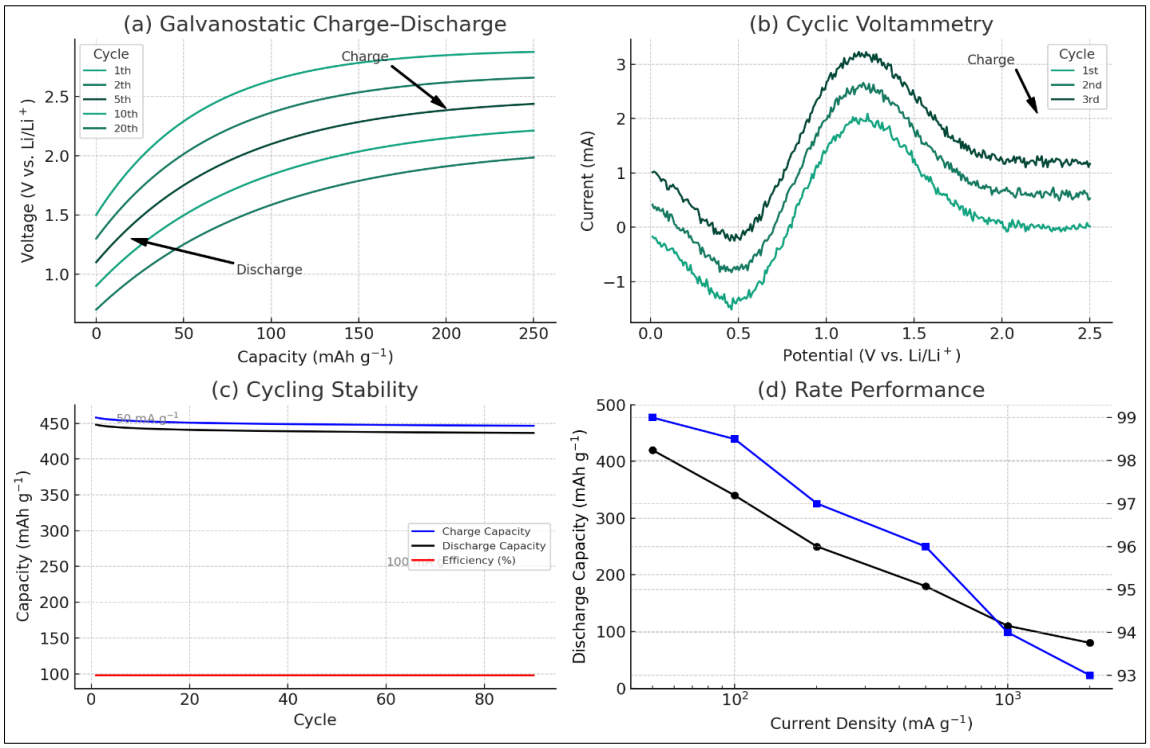

Figure 2: Electrochemical Performance of Cs_2NaBiI_6 Electrodes in Lithium-Ion Batteries

(a) Galvanostatic charge–discharge profiles measured in the voltage range of 2.5–0.01 V vs Li/Li^+ at 100 mA g^{-1} (with the initial 5 cycles at 50 mA g^{-1}), showing cycle numbers and charge/discharge directions. (b) Cyclic voltammetry of Cs_2NaBiI_6 vs Li metal for the first three cycles at a scan rate of 0.5 mV s^{-1}, highlighting the reversibility of lithium insertion/extraction. (c) Long-term cycling stability at 100 mA g^{-1} (after initial formation cycles), demonstrating sustained performance over 90 cycles. (d) Rate capability at increasing current densities, showing the retention of specific capacity. Measurement uncertainties for capacity and efficiency were less than ±0.1% throughout.

3.3. Mechanistic Insights into Lithiation/Delithiation and Photocharging Behavior

3.3.1. Electrochemical Mechanism via Cyclic Voltammetry and Ex Situ XRD

To understand the fundamental processes underpinning lithium storage in Cs_2NaBiI_6, cyclic voltammetry (CV) was performed within a potential window of 2.50–0.01 V versus Li/Li^+ at a scan rate of 0.5 mV s^{-1}. The first cathodic scan, depicted in Figure 2b, displays a broad and irreversible peak between 1.0 and 2.0 V, which disappears in subsequent cycles. This peak is characteristic of the initial formation of the solid electrolyte interphase (SEI) on the perovskite surface, and the simultaneous reduction of Bi^{3+} ions in Cs_2NaBiI_6 to metallic Bi^0. This conversion process is responsible for the irreversible capacity loss during the first cycle—a phenomenon also reported for other Bi-based electrodes [17,30,31].

In subsequent cycles, two pronounced cathodic peaks are observed at lower potentials (0.7 V and 0.5 V), consistent with the stepwise alloying of metallic Bi with lithium to form LiBi and Li_3Bi, respectively [30]. The sharp oxidation peak near 0.9 V arises from the dealloying reaction, wherein Li_3Bi is oxidized back to Bi^0 and Li^+. Notably, the potentials at which these transformations occur closely match the voltage plateaus

seen in the charge–discharge profiles, confirming the consistency between the CV and GCD data.

To further investigate the evolution of the crystal structure during cycling, ex situ X-ray diffraction (XRD) analysis was conducted at different stages of the first discharge (Figure S3a). Cells were discharged to specific potentials, carefully dismantled, and the electrodes were thoroughly rinsed with dimethyl carbonate (DMC) to eliminate residual electrolyte and salt [32], then dried before analysis. As shown in Figure S3b, the pristine electrode (2.5 V) exhibits peaks corresponding to Cs_2NaBiI_6. Upon discharge to 1.6 V, a new peak emerges at 27.26°, matching the (012) reflection of metallic Bi (JCPDS Card No. 85-1329), indicating the reduction of Bi^{3+}. Further lithiation to 0.64 V results in the appearance and intensification of LiBi and Li_3Bi phases, providing direct evidence for the conversion and alloying mechanisms proposed. This sequence of phase transformations is well-aligned with reports for other Bi-based electrode materials such as Bi_2Se_3, $BiVO_4$, and bismuth oxyhalides [30,33,34].

The multistep lithiation mechanism for Cs_2NaBiI_6 is summarized as follows:
(i) Intercalation: $Li^+ + Cs_2NaBiI_6 \rightarrow Li_xCs_2NaBiI_6$
(ii) Conversion: Bi^{3+} (in perovskite) + $3e^- \rightarrow Bi^0$
(iii) Alloying: $Bi^0 + Li^+ + e^- \rightarrow LiBi$
$LiBi + 2Li^+ + 2e^- \rightarrow Li_3Bi$

This mechanism explains both the high initial capacity and the stabilization of capacity over extended cycling, as the reversible alloying reactions dominate subsequent cycles while the initial irreversible processes account for the capacity loss in the first discharge.

3.3.2. Integration and Testing as a Photoelectrode

Following validation of electrochemical performance in standard Li-ion configuration, the role of Cs_2NaBiI_6 as a photoactive electrode in a photobattery (PHBAT) was explored. For efficient photocharging, the opaque copper current collector was replaced by porous carbon fiber (CF), which allows light transmission while maintaining good conductivity. The active layer was fabricated by blending Cs_2NaBiI_6, PCBM, and PVDF in a 70:20:10 weight ratio in NMP, and drop-casting onto the CF substrate (details in Supporting Information).

The morphology of the Cs_2NaBiI_6/CF electrode, visualized via SEM (Figure S4b), displays well-formed, hexagonal perovskite platelets embedded within the fibrous network of carbon paper—providing both structural robustness and a large interface for charge collection.

Initial battery tests with CF as the current collector, but without light (standard battery mode), show that CF contributes minimal capacity above 0.2 V, allowing accurate assessment of the Cs_2NaBiI_6 active layer. The first discharge at 100 mA g^{-1} yields an irreversible capacity of 540 mAh g^{-1}, again attributed to the initial conversion reaction and SEI formation. Remarkably, a stable reversible capacity of 270 mAh g^{-1} is maintained after 80 cycles (Figure S5), and the electrode demonstrates excellent rate capability with nearly 100% retention at 100 mA g^{-1} even after exposure to higher current densities (Figure S5d).

3.3.3. Photoelectrochemical Performance

The true multifunctionality of the device is revealed through photoelectrochemical experiments. Chronoamperometric measurements were carried out under alternating dark and illuminated (1 sun) conditions with an applied bias of 0 V versus Li/Li^+. As shown in Figure 3a, the current response increases instantly upon illumination and returns to baseline in the dark, confirming the rapid generation and extraction of photogenerated carriers in Cs_2NaBiI_6.

This light-driven charge storage is further demonstrated by powering a 1.5 V digital stopwatch using a PHBAT exclusively charged by light (Figure 3b), directly visualizing the device's practical utility. Additional cyclic voltammetry under dark and illuminated conditions (Figures 3c, 3d) and light/photocharging experiments (Figure 3e) reveal that the stored charge and discharge capacity can be tuned by the duration and intensity of light exposure (Figure 3f), providing a powerful platform for integrated solar energy harvesting and storage.

3.4. Photogenerated Charge Storage and Mechanistic Understanding in CF-PHBAT Devices

The unique electrochemical responses of the photo-rechargeable lithium-ion battery (PHBAT) were thoroughly analyzed under both dark and illuminated conditions using cyclic voltammetry (CV), as depicted in Figure 3c. During the initial cycle, a distinct irreversible cathodic peak above 1.0 V versus Li/Li^+ is evident, signaling the conversion of Bi^{3+} to metallic Bi^0 and the concurrent formation of a solid electrolyte interphase (SEI) on the electrode surface. This is consistent with the behavior observed in conversion-type Bi-based anodes and indicates the substantial irreversible capacity loss associated with these initial processes. Importantly, the use of a carbon fiber (CF) current collector in place of copper (Cu) necessitated narrowing the voltage window to 2.5–0.2 V versus Li/Li^+, as CF exhibits significant reactivity with lithium at lower potentials. This adjustment ensures that critical electrochemical phenomena in the Cs_2NaBiI_6 photoelectrode can be observed with minimal interference from the current collector itself.

A striking enhancement in current is observed in both cathodic and anodic sweeps under white light illumination, a direct consequence of increased photogeneration of charge carriers and photocharging effects. In subsequent cycles, as seen in Figure 3d, the previously observed irreversible peak disappears,

replaced by well-defined, reversible alloying and dealloying peaks. The amplification of these Li–Bi reaction peaks under illumination not only demonstrates improved charge transfer kinetics but also suggests that photogenerated electrons participate directly in the redox reactions, confirming the intrinsic photosensitivity of the Cs_2NaBiI_6 active layer. The consistent appearance of these features from the fourth cycle onward under both light and dark conditions further suggests that these improvements are a bulk property of the electrode material, not merely a surface phenomenon.

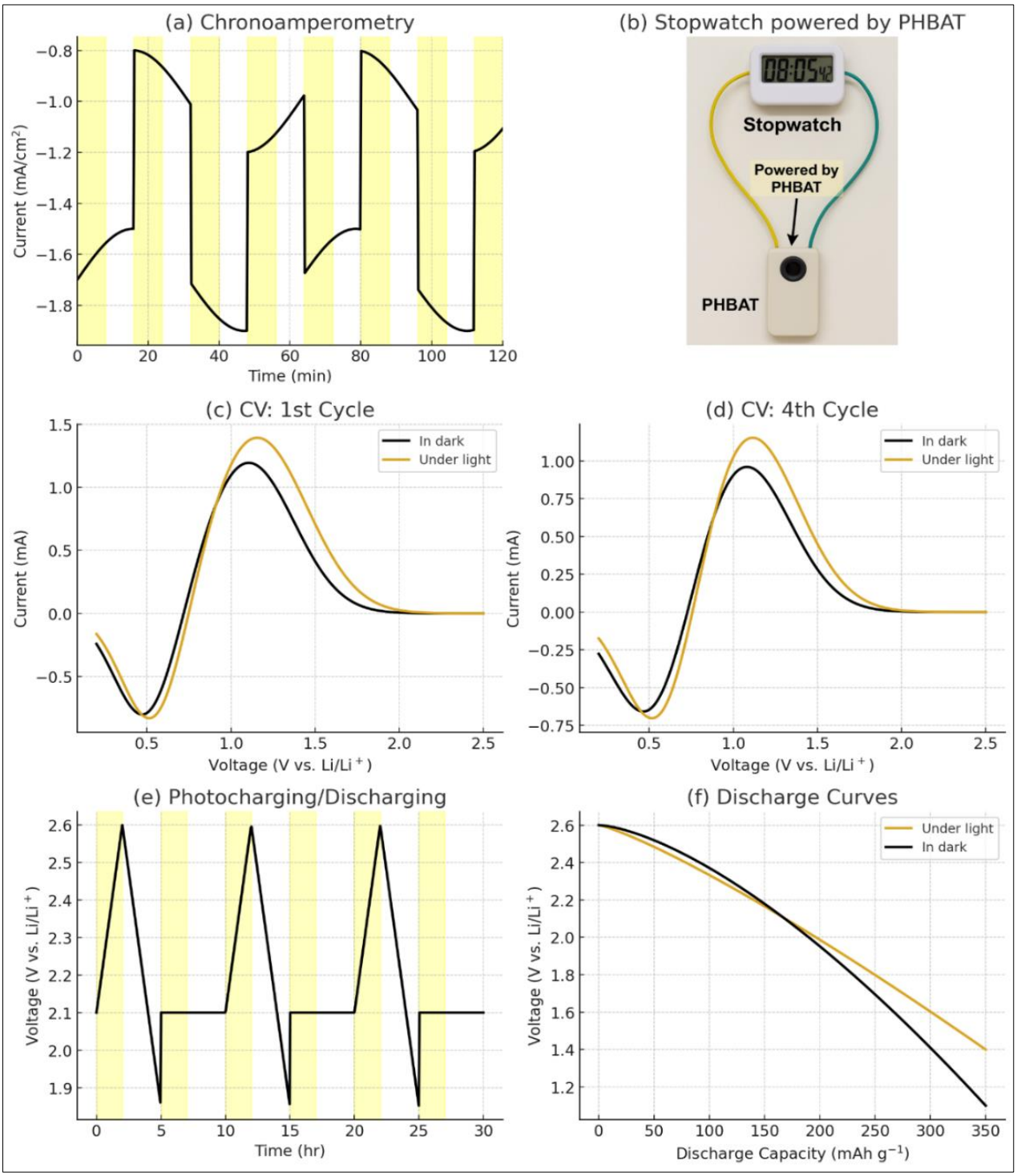

Figure 3: Photoelectrochemical Analysis of Cs_2NaBiI_6-Based Photobattery. (a) Chronoamperometric response under alternating dark/light cycles, showing rapid and reversible photoresponse at 0 V vs Li/Li^+. (b) A digital stopwatch powered by a PHBAT charged solely by light. (c, d) CV curves under dark and light (1 sun) conditions for the 1st and 4th cycles, respectively. (e) Battery charging under illumination (yellow region), with red lines indicating photocharging, black lines for galvanostatic discharge in the dark, and green lines for rest. (f) Discharge curves demonstrating light-dependent capacity modulation under constant current (100 mA g^{-1}).

3.4.1. Light-Driven Charging and Capacity Modulation

The light-induced charging performance of the PHBAT was subsequently evaluated in the absence of any external current input. After a brief period of photocharging under 1 sun illumination, the open circuit voltage (OCV) was measured and the battery was then discharged galvanostatically in the dark at 100 mA g^{-1} (Figure 3e). To mitigate potential degradation arising from excessive Li–Bi alloy formation at very low voltages, the discharge was limited to 0.9 V. This protocol was repeated for seven cycles, each demonstrating successful photocharging, as evidenced by only minimal voltage drops during the discharge phases. Notably, extended photocharging under continuous illumination led to a steady rise in cell voltage, surpassing 2.9 V. Once the light source was removed, a sudden voltage drop was observed, confirming that the increased potential was attributable to the photogenerated charge carriers within the device.

This set of experiments enables direct calculation of the light-conversion efficiency (LCE), which was determined to be 0.27% for the "first charge" in the top-performing PHBAT device under 1 sun illumination (see Figure S7 and Table S1). This value exceeds the LCEs reported for most previously published photo-rechargeable perovskite lithium-ion batteries (generally in the range of 0.03–0.22%) [8,9,14,35], although it is slightly lower than the best-performing $Cs_3Bi_2I_9$-based device reported previously [17]. Nevertheless, the present Cs_2NaBiI_6 PHBAT demonstrates higher capacity, superior rate performance, and markedly improved cycling stability, with a (non-photo) discharge capacity of 152 mAh g^{-1} after 90 cycles—compared to only 47 mAh g^{-1} for $Cs_3Bi_2I_9$ under similar conditions [17].

A direct comparison of PHBATs discharged under illumination and in darkness (Figure 3f) reveals a substantial increase in capacity for the light-charged cell, which reached over 1000 mAh g^{-1} after extended illumination (24 hours) versus 566 mAh g^{-1} in the dark. This enhancement arises from the simultaneous processes of photocharging and galvanostatic discharging: under continuous light, the photogenerated charges contribute to the battery's capacity in real time. In principle, the delivered capacity can be extended nearly arbitrarily with increased illumination time, as the rate of photostorage approaches the rate of discharge. Once illumination ceases, the battery resumes normal discharge characteristics.

3.4.2. Mechanistic Insights: Photocharging Pathways

The mechanisms underlying photocharging in CF-PHBATs are summarized in Figure 4 and are broadly consistent with previous models of photo-rechargeable perovskite systems [8,14]. Upon illumination with photons possessing energies greater than the Cs_2NaBiI_6 band gap, photogenerated electrons migrate through PCBM to the CF current collector, enabled by favorable band alignment. Meanwhile, holes remain in the perovskite valence band and may either drive delithiation of the active layer—thus regenerating the charged state via Li^+ release into the electrolyte—or, at lower potentials, oxidize metallic Bi^0 back to Bi^{3+} [36]. Both processes contribute to photocharging and restore the cell's capacity for subsequent discharges.

Transient absorption (TA) spectroscopy (see Figure S8) provides further evidence for these processes, revealing extended lifetimes for photogenerated carriers in Cs_2NaBiI_6/PCBM composites compared to PCBM or polymer alone, supporting efficient charge separation and utilization. Multiple electronic pathways exist for photogenerated electrons: they may travel through the external circuit to reduce Li^+ at the counter electrode, or they may react with EC/DMC solvent to generate reactive oxygen species (ROS), which in turn promote SEI formation on the Li metal [8,9]. Figure 4c provides a schematic representation of this alternative pathway.

Despite the theoretical need for an external circuit to complete Li^+ reduction to metallic Li, the substantial reservoir of Li metal in the device permits sustained photocharging and reversible operation over numerous cycles without external intervention. Thus, CF-PHBATs represent a robust platform for integrated solar energy harvesting and storage, with the potential for high capacities, excellent stability, and tunable output governed by light exposure.

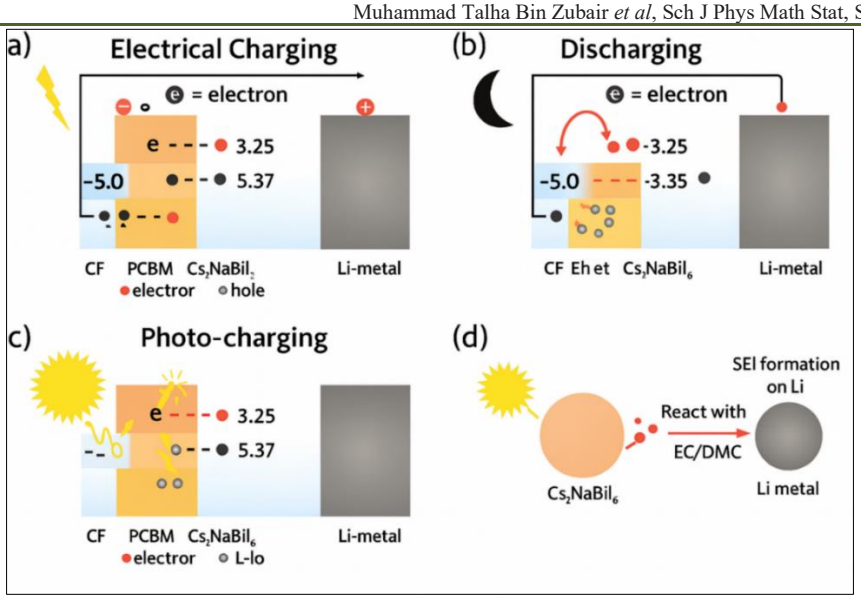

Figure 4: Photocharging Mechanisms in CF-PHBAT. (a) Schematic illustration of the photocharging process for Cs_2NaBiI_6, showing electron and hole pathways under illumination. (b) Discharge mechanism highlighting Li^+ insertion and Bi redox chemistry. (c) Alternative pathway for SEI formation via photo-induced ROS generation at the Li metal electrode. (d) Mechanism of photogenerated electron reaction and charge transfer in the open circuit state.

4. CONCLUSION

In summary, this study demonstrates for the first time the successful application of the lead-free double-perovskite halide Cs_2NaBiI_6 as both an efficient electrode and a photoactive electrode in lithium-ion photobatteries (PHBATs). The synthesized Cs_2NaBiI_6 exhibits outstanding electrochemical performance, with a high initial specific capacity of 450 mAh g^{-1} and excellent cycling stability, retaining 150 mAh g^{-1} even after 90 cycles and remaining operational with stable output for up to 500 cycles. Ex situ X-ray diffraction studies provide direct evidence that the lithium storage mechanism is governed by a sequential process, beginning with the reduction of Bi^{3+} to metallic Bi^0, followed by alloying to form LiBi and Li_3Bi phases during discharge.

The photo-rechargeable batteries based on Cs_2NaBiI_6 achieve a maximum light conversion efficiency (LCE) of 0.27% during the initial discharge, ranking among the highest efficiencies reported for lithium-ion perovskite photobatteries under standard solar illumination. Chronoamperometry studies further confirm the material's robust photoactivity, with substantial increases in current response under illumination and clear evidence of photocharging through alternate dark/light cycling. Notably, the device demonstrates a pronounced enhancement in discharge capacity when cycled under light compared to dark conditions, confirming that photogenerated carriers significantly contribute to the overall energy storage process.

The practical utility of the PHBAT is showcased by its ability to power a 1.5 V digital stopwatch for several minutes, charged solely by incident light, thus highlighting the potential for real-world applications in self-powered, sustainable electronic devices. When benchmarked against previously studied $Cs_3Bi_2I_9$-based photobatteries, Cs_2NaBiI_6 exhibits superior specific capacity (152 vs 47 mAh g^{-1} after 90 cycles in non-photo mode), improved rate performance, and remarkable long-term cycling stability.

These advances establish Cs_2NaBiI_6 as a highly promising, environmentally friendly candidate for the next generation of high-performance photo-rechargeable lithium-ion batteries, opening new avenues for integrated solar energy harvesting and storage solutions. Future research focused on further optimizing the photoelectrode architecture, exploring alternative double perovskite compositions, and scaling up device integration could accelerate the development of practical photobattery systems for renewable energy applications.

REFERENCES

1. Vlad, A.; Singh, N.; Galande, C.; Ajayan, P. M. Design considerations for unconventional electrochemical energy storage architectures. *Adv. Energy Mater.* 2015, *5* (19), 1402115. https://doi.org/10.1002/aenm.201402115
2. Tewari, N.; Lam, D.; Li, C. H. A.; Halpert, J. E. Recent advancements in batteries and photo-batteries using metal halide perovskites. *APL Mater.* 2022, *10* (4), 040905. https://doi.org/10.1063/5.0086599
3. Yun, S.; Zhang, Y.; Xu, Q.; Liu, J.; Qin, Y. Recent advance in new-generation integrated devices for energy harvesting and storage. *Nano Energy* 2019, *60*, 600–619. https://doi.org/10.1016/j.nanoen.2019.03.074

4. Lee, A.; Vörös, M.; Dose, W. M.; Niklas, J.; Poluektov, O.; Schaller, R. D.; Iddir, H.; Maroni, V. A.; Lee, E.; Ingram, B.; Curtiss, L. A.; Johnson, C. S. Photo-accelerated fast charging of lithium-ion batteries. *Nat. Commun.* 2019, *10* (1), 1–7. https://doi.org/10.1038/s41467-019-12863-6
5. Yu, M.; Ren, X.; Ma, L.; Wu, Y. Integrating a redox-coupled dye-sensitized photoelectrode into a lithium-oxygen battery for photoassisted charging. *Nat. Commun.* 2014, *5* (1), 1–6. https://doi.org/10.1038/ncomms6111
6. Boruah, B. D.; Mathieson, A.; Wen, B.; Feldmann, S.; Dose, W. M.; De Volder, M. Photo-rechargeable zinc-ion batteries. *Energy Environ. Sci.* 2020, *13* (8), 2414–2421. https://doi.org/10.1039/D0EE01392G
7. Hodes, G.; Manassen, J.; Cahen, D. Photoelectrochemical energy conversion and storage using polycrystalline chalcogenide electrodes. *Nature* 1976, *261* (5559), 403–404. https://doi.org/10.1038/261403a0
8. Ahmad, S.; George, C.; Beesley, D. J.; Baumberg, J. J.; De Volder, M. Photo-rechargeable organo-halide perovskite batteries. *Nano Lett.* 2018, *18* (3), 1856–1862. https://doi.org/10.1021/acs.nanolett.7b05153
9. Paolella, A.; Faure, C.; Bertoni, G.; Marras, S.; Guerfi, A.; Darwiche, A.; Hovington, P.; Commarieu, B.; Wang, Z.; Prato, M. Light-assisted delithiation of lithium iron phosphate nanocrystals towards photo-rechargeable lithium ion batteries. *Nat. Commun.* 2017, *8* (1), 1–10. https://doi.org/10.1038/ncomms14643
10. Paolella, A.; Vijh, A.; Guerfi, A.; Zaghib, K.; Faure, C. Li-ion photo-batteries: challenges and opportunities. *J. Electrochem. Soc.* 2020, *167* (12), 120545. https://doi.org/10.1149/1945-7111/abb178
11. Narayanan, N. T.; Kumar, A.; Thakur, P.; Sharma, R.; Puthirath, A.; Pulickel, A. Photo rechargeable Li-ion batteries using nanorod heterostructure electrodes. *Small* 2021, *17* (51), 2105029. https://doi.org/10.1002/smll.202105029
12. Rodríguez-Seco, C.; Wang, Y.-S.; Zaghib, K.; Ma, D. Photoactive nanomaterials enabled integrated photo-rechargeable batteries. *Nanophotonics* 2022, *11* (8), 1443–1484. https://doi.org/10.1515/nanoph-2021-0782
13. Salunke, A. D.; Chamola, S.; Mathieson, A.; Boruah, B. D.; de Volder, M.; Ahmad, S. Photo-rechargeable Li-ion batteries: device configurations, mechanisms, and materials. *ACS Appl. Energy Mater.* 2022, *5* (7), 7891–7912. https://doi.org/10.1021/acsaem.2c01109
14. Boruah, B. D.; Wen, B.; De Volder, M. Light rechargeable lithium-ion batteries using V_2O_5 cathodes. *Nano Lett.* 2021, *21* (8), 3527–3532. https://doi.org/10.1021/acs.nanolett.1c00298
15. Zhang, L.; Miao, J.; Li, J.; Li, Q. Halide perovskite materials for energy storage applications. *Adv. Funct. Mater.* 2020, *30* (40), 2003653. https://doi.org/10.1002/adfm.202003653
16. Liang, S.; Zhang, M.; Biesold, G. M.; Choi, W.; He, Y.; Li, Z.; Shen, D.; Lin, Z. Recent advances in synthesis, properties, and applications of metal halide perovskite nanocrystals/polymer nanocomposites. *Adv. Mater.* 2021, *33* (50), 2005888. https://doi.org/10.1002/adma.202005888
17. Tewari, N.; Shivarudraiah, S. B.; Halpert, J. E. Photorechargeable lead-free perovskite lithium-ion batteries using hexagonal $Cs_3Bi_2I_9$ nanosheets. *Nano Lett.* 2021, *21* (13), 5578–5585. https://doi.org/10.1021/acs.nanolett.1c01000
18. Chu, L.; Ahmad, W.; Liu, W.; Yang, J.; Zhang, R.; Sun, Y.; Yang, J.; Li, X. Lead-free halide double perovskite materials: a new superstar toward green and stable optoelectronic applications. *Nanomicro Lett.* 2019, *11*, 1–18. https://doi.org/10.1007/s40820-019-0244-6
19. Meyer, E.; Mutukwa, D.; Zingwe, N.; Taziwa, R. Lead-free halide double perovskites: a review of the structural, optical, and stability properties as well as their viability to replace lead halide perovskites. *Metals* 2018, *8* (9), 667. https://doi.org/10.3390/met8090667
20. Usman, M.; Yan, Q. Recent advancements in crystalline Pb-free halide double perovskites. *Crystals* 2020, *10* (2), 62. https://doi.org/10.3390/cryst10020062
21. Yang, X.; Wang, W.; Ran, R.; Zhou, W.; Shao, Z. Recent advances in $Cs_2AgBiBr_6$-based halide double perovskites as lead-free and inorganic light absorbers for perovskite solar cells. *Energy Fuels* 2020, *34* (9), 10513–10528. https://doi.org/10.1021/acs.energyfuels.0c02236
22. Kangsabanik, J.; Sugathan, V.; Yadav, A.; Yella, A.; Alam, A. Double perovskites overtaking the single perovskites: a set of new solar harvesting materials with much higher stability and efficiency. *Phys. Rev. Mater.* 2018, *2* (5), 055401. https://doi.org/10.1103/PhysRevMaterials.2.055401
23. Yang, S.; Liang, Q.; Wu, H.; Pi, J.; Wang, Z.; Luo, Y.; Liu, Y.; Long, Z.; Zhou, D.; Wen, Y. Lead-free double perovskite $Cs_2NaErCl_6$: Li^+ as high-stability anodes for Li-ion batteries. *J. Phys. Chem. Lett.* 2022, *13* (22), 4981–4987. https://doi.org/10.1021/acs.jpclett.2c01052
24. Wu, H.; Pi, J.; Liu, Q.; Liang, Q.; Qiu, J.; Guo, J.; Long, Z.; Zhou, D.; Wang, Q. All-inorganic lead free double perovskite Li-battery anode material hosting high Li^+ ion concentrations. *J. Phys. Chem. Lett.* 2021, *12* (17), 4125–4129. https://doi.org/10.1021/acs.jpclett.1c00041
25. Prabhu, K.; Chandiran, A. K. Solar energy storage in a $Cs_2AgBiBr_6$ halide double perovskite photoelectrochemical cell. *Chem. Commun.* 2020, *56* (53), 7329–7332. https://doi.org/10.1039/D0CC02743J
26. Boruah, B. D.; Wen, B.; De Volder, M. Molybdenum disulfide-zinc oxide photocathodes for photo-rechargeable zinc-ion batteries. *ACS Nano*

2021, *15* (10), 16616–16624. https://doi.org/10.1021/acsnano.1c06372

27. Zhang, C.; Gao, L.; Teo, S.; Guo, Z.; Xu, Z.; Zhao, S.; Ma, T. Design of a novel and highly stable lead-free Cs_2NaBiI_6 double perovskite for photovoltaic application. *Sust. Energy Fuels* 2018, *2* (11), 2419–2428. https://doi.org/10.1039/C8SE00154E
28. Li, P.; Gao, W.; Ran, C.; Dong, H.; Hou, X.; Wu, Z. Post-treatment engineering of vacuum-deposited Cs_2NaBiI_6 double perovskite film for enhanced photovoltaic performance. *Phys. Stat. Solidi (A)* 2019, *216* (23), 1900567. https://doi.org/10.1002/pssa.201900567
29. Zhao, X.-G.; Yang, J.-H.; Fu, Y.; Yang, D.; Xu, Q.; Yu, L.; Wei, S.-H.; Zhang, L. Design of lead-free inorganic halide perovskites for solar cells via cation-transmutation. *J. Am. Chem. Soc.* 2017, *139* (7), 2630–2638. https://doi.org/10.1021/jacs.6b09645
30. Jin, Y.; Yuan, H.; Lan, J.-L.; Yu, Y.; Lin, Y.-H.; Yang, X. Bio-inspired spider-web-like membranes with a hierarchical structure for high performance lithium/sodium ion battery electrodes: the case of 3D freestanding and binder-free bismuth/CNF anodes. *Nanoscale* 2017, *9* (35), 13298–13304. https://doi.org/10.1039/C7NR04912A
31. Zhong, Y.; Li, B.; Li, S.; Xu, S.; Pan, Z.; Huang, Q.; Xing, L.; Wang, C.; Li, W. Bi nanoparticles anchored in N-doped porous carbon as anode of high energy density lithium ion battery. *Nanomicro Lett.* 2018, *10* (4), 1–14. https://doi.org/10.1007/s40820-018-0209-1
32. Waldmann, T.; Iturrondobeitia, A.; Kasper, M.; Ghanbari, N.; Aguesse, F.; Bekaert, E.; Daniel, L.; Genies, S.; Gordon, I. J.; Löble, M. W. Post-mortem analysis of aged lithium-ion batteries: disassembly methodology and physico-chemical analysis techniques. *J. Electrochem. Soc.* 2016, *163* (10), A2149. https://doi.org/10.1149/2.1211609jes
33. Wang, A.; Hong, W.; Yang, L.; Tian, Y.; Qiu, X.; Zou, G.; Hou, H.; Ji, X. Bi-based electrode materials for alkali metal-ion batteries. *Small* 2020, *16* (48), 2004022. https://doi.org/10.1002/smll.202004022
34. Dai, S.; Wang, L.; Shen, Y.; Wang, M. Bismuth selenide nanocrystalline array electrodes for high-performance sodium-ion batteries. *Appl. Mater. Today* 2020, *18*, 100455. https://doi.org/10.1016/j.apmt.2019.100455
35. Kumar, A.; Thakur, P.; Sharma, R.; Puthirath, A. B.; Ajayan, P. M.; Narayanan, T. N. Photo rechargeable Li-ion batteries using nanorod heterostructure electrodes. *Small* 2021, *17* (51), 2105029. https://doi.org/10.1002/smll.202170270
36. Cheng, X.; Li, D.; Jiang, Y.; Huang, F.; Li, S. Advances in electrochemical energy storage over metallic bismuth-based materials. *Materials* 2024, *17* (1), 21. https://doi.org/10.3390/ma17010021
37. Tailor, N. K.; Listorti, A.; Colella, S.; Satapathi, S. Lead-free halide double perovskites: fundamentals, challenges, and photovoltaics applications. *Adv. Mater. Technol.* 2023, *8* (1), 2200442. https://doi.org/10.1002/admt.202200442
38. Malik, A., Liaqat, M., ur Rahman, M., Shafique, A. Y., Haseeb, M., & Ahmad, S. Nanotechnology for Perovskite Solar Cells: Solving Efficiency, Stability, and Energy Storage Challenges.
39. Nazar, M. (2025). DFT Study of Optoelectronic and Thermoelectric Properties of Halide Double Perovskite Rb_2TlSbX_2 (X= Cl, Br, I) for Solar Cell Applications. Sch J Eng Tech, 4, 208-222.
40. Iqbal, M. T., Saeeda, S., Zahra, T., Umar, Z., Khan, W. Z., Adnan, M., ... & Toffique, M. (2025). Next-Generation Materials Discovery Using DFT: Functional Innovation. Solar Energy, Catalysis, and Eco Toxicity Modelling. Sch J Eng Tech, 7, 454-486.
41. Mudassar, M. A., Khalid, A., Ashraf, A., Barkat, U., Aslam, M. A., Talha, H. M., ... & Khan, W. Z. (2025). Theoretical Design and Optoelectronic Analysis of Lead-Free $CsPbX_3/Cs_2SnX_6$ Core–Shell Perovskite Nanocrystals for Enhanced Stability and Charge Dynamics. Sch J Phys Math Stat, 6, 226-239.
42. Nazar, M., Younis, B., Akbar, H., Ahmad, S., Rustam, R., Akram, I., & Munir, F. (2024). Advancing Perovskite Solar Cells: Addressing Stability, Scalability, and Environmental Challenges. Dialogue Social Science Review (DSSR), 2(4), 395-422.